

Kinematics of the Narrow-Line Region in the Seyfert 2 Galaxy NGC 1068: Dynamical Effects of the Radio Jet¹

V. Das², D.M. Crenshaw², S.B. Kraemer³, R. P. Deo²

Received _____; accepted _____

¹Based on observations made with the NASA/ESA Hubble Space Telescope. STScI is operated by the Association of Universities for Research in Astronomy, Inc., under NASA contract NAS5-26555.

²Department of Physics and Astronomy, Georgia State University, Astronomy Offices, One Park Place South SE, Suite 700, Atlanta, GA 30303, das@chara.gsu.edu, crenshaw@chara.gsu.edu, deo@chara.gsu.edu

³Catholic University of America and Laboratory for Astronomy and Solar Physics, NASA's Goddard Space Flight Center, Code 681, Greenbelt, MD 20771, stiskraemer@yancey.gsfc.nasa.gov.

ABSTRACT

We present a study of high-resolution long-slit spectra of the narrow-line region (NLR) in NGC 1068 obtained with the Space Telescope Imaging Spectrograph (STIS) aboard *The Hubble Space Telescope (HST)*. The spectra were retrieved from the Multimission Archive at Space Telescope (MAST) obtained from two visits and seven orbits of *HST* time. We also obtained MERLIN radio maps of the center of NGC 1068 to examine the dependence of the NLR cloud velocities on the radio structure. The radial velocities and velocity dispersions of the bright NLR clouds appear to be unaffected by the radio knots, indicating that the radio jet is not the principal driving force on the outflowing NLR clouds. However, the velocities of the fainter NLR clouds are split near knots in the jet, indicating a possible interaction. Biconical outflow models were generated to match the data and for comparison to previous models done with lower dispersion observations. The general trend is an increase in radial velocity roughly proportional to distance from the nucleus followed by a linear decrease after roughly 100 parsec similar to that seen in other Seyfert galaxies, indicating common acceleration/deceleration mechanisms.

Subject headings: galaxies: kinematics and dynamics – galaxies: individual (NGC 1068) galaxies: Seyfert – AGN: emission lines – ultraviolet: galaxies

1. Introduction

NGC 1068 is classified as a Seyfert type 2 active galaxy because of its narrow (FWHM $\approx 500 \text{ km s}^{-1}$) permitted and forbidden optical emission lines and its weak underlying non-thermal continuum. However from spectropolarimetry studies, Antonucci & Miller (1985) discovered a featureless continuum and broad (FWHM $\approx 3000 \text{ km s}^{-1}$) permitted lines in the core of NGC 1068, similar to the spectrum of Seyfert 1s. Their conclusion was that the central continuum source and broad line region (BLR) in NGC 1068 is hidden behind a geometrically and optically thick dusty torus. Subsequent studies by Miller & Goodrich (1990) found that four out of eight previously classified Seyfert 2 galaxies revealed hidden Seyfert 1 nuclei and Kay (1994) identified additional Seyfert 1 nuclei in a spectropolarimetric study of a large sample of Seyfert 2 galaxies. The unification model seems stronger than ever after several more authors found hidden broad-line regions in Seyfert 2 cores (Tran et al. 1992; Young et al. 1993, 1996; Moran et al. 2000; Tran 2001; Lumsden et al. 2001). More recent spectropolarimetric studies by Zakamska et al. (2005) on Type II Quasars, the luminous analogs of Seyfert 2 galaxies, further compliment the unification model of active galactic nuclei (AGN). They found that five out of the 12 studied objects showed broad lines. Although it is generally accepted that the two classes of Seyfert galaxies harbor the same type of nucleus that are seen differently because of viewing angle, it remains to be shown that they are indeed one and the same. The ability of our models to match the data of both Seyfert types provides yet another piece of compelling evidence for the unification scheme.

The ionization mechanism of the NLR of Seyfert galaxies has been scrutinized intensely over the past few decades. The two leading mechanisms were photoionization (see Koski 1978; Ferland & Osterbrock 1986, and references therein) and shock ionization (see Dopita

& Sutherland 1995, and references therein). Photoionization was suggested as the dominant source of energy to produce the emission lines seen in the NLR as early as 1964 (Greenstein & Schmidt 1964; Oke 1965), where it was shown that shocks would not suffice to produce continuous energy in a small region over large timescales. Models by Osterbrock & Parker (1966) showed that photoionization can account for both high and low ionization emission lines seen in QSOs.

Recently, studies have shown that most of the emission lines seen in the NLR can be accounted for by assuming a central ionization source illuminating a multi-component gas (Kraemer et al. 2000; Kraemer & Crenshaw 2000a; Groves et al. 2004, and references therein), although an additional localized source of ionization in NGC 1068 was detected, which may be due to shocks, at the point where the NLR gas decelerates. This kind of shock may be caused by the interaction of NLR clouds with diffuse plasma in the ambient medium, providing the drag in our kinematic models (Kraemer & Crenshaw 2000b). Mundell et al. (2003) showed that the misalignment of the radio jet and NLR in NGC 4151 supports photoionization of the NLR by the AGN as the dominant excitation mechanism, but that enhanced optical emission observed in a few clouds bounding the radio jet might be shock related. Since it is now generally accepted that photoionization is the dominant source of ionization of the NLR gas, with shocks possibly contributing in localized regions, we will focus our paper on kinematic models to gain more insight into how these sources of energy may affect the acceleration of the gas.

With the launch of *HST* and its high angular resolution ($0''.1$), the NLR of Seyfert galaxies has received considerable attention. With the long-slit capability of the Space Telescope Imaging Spectrograph, and the Faint Object Camera (FOC), detailed constraints on kinematic models of the NLR in the two types of Seyfert galaxies became possible. In turn, these models provide good diagnostics upon which dynamical analyzes can be based.

One such kinematic study of the NLR clouds is provided in this paper as a tool for this endeavor. We used a systemic redshift of NGC 1068 of 1148 km s^{-1} from HI measurements by Brinks et al. (1997) and a distance of 14.4 Mpc (Bland-Hawthorn et al. 1997), so that $0''.1$ corresponds to 7.2 pc.

1.1. Lateral Expansion away from the Radio Jets

Based on FOC long-slit spectra, several authors suggest that the NLR clouds are accelerated by shocks generated by interactions between a radio jet and the ISM, such that clouds are carried away laterally from the jet axis by an expanding cocoon of shocked gas (Axon et al. 1998; Capetti et al. 1999, and references therein). In Capetti et al. (1999), long slit FOC spectra were taken perpendicular to the radio jet of Mrk 3. They found that in some slits, the [OIII] emission line velocities split into two systems separated by several hundreds km s^{-1} apart on either side of the jet. One of the systems is receding and the other one is approaching relative to the host systemic velocity, which Capetti et al. (1999) interpreted as expansion of gas away from the jet. In Axon et al. (1998) the same splitting of velocities across a radio jet was observed in NGC 1068 and also interpreted as expansion of the gas away from the radio jet. The jet-driven models suggest that the lateral expansion of the shocked cocoon will produce both blueshifted and redshifted velocities with approximately equal magnitudes along the jet/bicone axis at each location in the NLR, regardless of axis orientation. A clear representation of this picture is shown in Figure 6 in Nelson et al. (2000).

The above model fails to explain the velocity structure in the NLR of NGC 4151, where STIS spectra revealed that primarily blueshifts were observed on the southwest side of the bicone and primarily redshifts on the southeast side (Das et al. 2005, and references therein). We noted in Das et al. (2005) that acceleration of some co-spatial clouds started well before any radio knot, and extended well across the knot, making it very unlikely that the knots

accelerate these clouds. Furthermore, in Das et al. (2005), we found many more [OIII] knots than radio knots in NGC 4151 and the clouds seem to accelerate even in the absence of any radio material, and in cases where there is radio material, the velocities of the clouds seem to be unaffected. We will see in this paper that there are possible interactions between radio and [OIII] knots in NGC 1068, but that these interactions are modest.

1.2. Radial-Outflow Models

Evidence of radial outflow in the NLR of NGC 1068 was first presented in ground based studies by Walker (1968), and subsequently by other researchers (e.g, Arribas et al. 1996; Cecil et al. 2002). Evidence for a biconical structure is expected from a simple unified model, due to collimation by a thick torus, (Antonucci & Miller 1985), and was seen by Pogge (1988). A sample of Seyfert 1s and 2s were compared to test the similarity of both NLR morphologies in Schmitt & Kinney (1996); they found biconical structures in most of their Seyfert 2s. Both Schulz (1990) and Evans et al. (1993) have modeled the NLR of NGC 4151 and found it to consistent with a biconical geometry.

Biconical outflow modeling of the NLR using STIS data was previously done by our group for NGC 1068 (Seyfert 2), Mrk 3 (Seyfert 2), and NGC 4151 (Seyfert 1). The NLR of NGC 1068 was modeled with data taken with the G430L grating of STIS and the radial velocity measurements were made using the bright [OIII] $\lambda 5007$ emission with a slit at position angle 202° and $0''.1$ wide (Crenshaw & Kraemer 2000b). Acceleration of the gas to ~ 100 pc and subsequent deceleration back to systemic velocity was clearly seen. The model consisted of a simple biconical outflow geometry which is evacuated along the axis and tilted slightly out of the plane of the sky to match the amplitudes of blueshifted and redshifted clouds. Blueshifted and redshifted clouds were observed in both the northeast and southwest parts of the bicone, which explains the “line-splitting” observed by Axon et al. (1998). The NLR

of Mrk 3 was modeled by Ruiz et al. (2001), using a combination of STIS medium resolution slitless and low resolution long slit data, and a similar geometrical model matched the data well. Clouds were seen to accelerate close to the nucleus, then decelerate back to systemic velocity, a trend which is seen in other Seyfert galaxies. In Crenshaw et al. (2000), the NLR of NGC 4151 was similarly modeled with two slit positions, each $0''.1$ wide, at position angles 221° and 70° . The axis of the bicone was tilted to match the blueshifted and redshifted clouds, which contrary to NGC 1068, occurred exclusively in the southwest and northeast bicones respectively. With an inclination of the bicone axis with respect to the plane of the sky of 40° , the models fit the data reasonably well. In Das et al. (2005), we modeled the NLR of NGC 4151 using five parallel slits at much higher spectral resolution ($\lambda/\Delta\lambda \sim 9000$). The slits were each $52'' \times 0''.2$ positioned at 58° and covering most of the NLR. The data allowed multiple [OIII] components to be detected and measured. The previous model from Crenshaw & Kraemer (2000b) was then fine-tuned to allow a better fit. The models were also consistent with the different slit position angles.

In an analysis of 10 Seyfert galaxies by Ruiz et al. (2005), we studied the kinematics of the NLR using slitless spectroscopy at high spectral resolution. The sample includes eight Seyfert 2, one Seyfert 1.9, and one Seyfert 1 galaxy. Each was observed with the STIS 1024 x 1024 pixel CCD detector through an open aperture ($52'' \times 52''$) and dispersed with the G430M grating. A high resolving power of ~ 9000 allowed us velocity measurements down to ~ 33 km s $^{-1}$ in the vicinity of the [OIII] $\lambda 5007$ line. Each target was observed during a single *HST* orbit. Although modeling was not done, the tell tale signs of acceleration/deceleration of the gas seemed to be present in almost all of their Seyferts. In all the above papers, the observations and models indicate that the dominant accelerating mechanism emanates from within tens of parsecs from the central engine and that the acceleration is radial rather than lateral (from the jet axis).

1.3. Kinematics of the NLR of NGC 1068 at High Spectral Resolution

Observations of NGC 1068 were taken on 1999 September, 1999 October, and 2000 September by Cecil et al. (2002). They used STIS aboard *HST* to obtain spectra with the G430M grating, at a spectral resolution of $\lambda/\Delta\lambda \approx 9000$ and a spatial resolution of $0''.1$ along and $0''.2$ across each slit. Due to complications with guide stars, the observing time was split into two parts, one year apart, which resulted in a total of seven parallel long slit spectra at position angle 38° . Slits 1–5 were taken in 1999, and slits 6–7 were taken the following year. However slits 5 and 6 contained the same region, except for an offset along the slits. The spectra from each slit had a spectral coverage of 4820–5100 Å, to obtain maps of the [OIII] and $H\beta$ profiles (for more details see Cecil et al. 2002). An additional observation with the G430M grating (slit 8) was taken by Antonucci (PI) in 2000 January at position angle of 10° .

Cecil et al. analyzed several complexes and knots of gas that cover the entire NLR. These were sampled into radial velocity profiles with some knots showing radial velocities as high as -3200 km s^{-1} . Simple biconical outflow models were overlaid on their [OIII] spectral images for all slit positions, and velocities were compared. They also overplotted model velocities where the gas is allowed to expand away from the radio jet axis. They found that a higher maximum velocity was required to better match the blue wing of the northeast bicone. The red wing was not matched. The lateral expansion model also predicted larger velocities for the red wings than the data. They suggest that the redshifted bright emission seen in the northeast cone is caused by the clouds being pushed into the galactic disk by the expansion of the radio lobe, and that these clouds are most likely dragged along the galactic disk. This may explain the clouds’s lower velocities. The blueshifted clouds are accelerated away from the galaxy and suffer no such fate and hence their higher velocities. They also suggest that the high-velocity knots in the northeast can be explained by ablation of massive

infalling dusty clouds.

We have remeasured Cecil et al.’s data specifically for testing simple velocity models, by separating the multiple emission components seen along the slit. As in Das et al. (2005), we wanted to test the relations among the different components and also to check for unusual flow patterns of the faint clouds as seen in the NLR of NGC 4151. We also wanted to test for radio/[OIII] interactions by comparing co-spatial slit coverage of optical emission data from Cecil et al. (2002) and radio emission from Gallimore et al. (2004).

2. Observations

The top panel of Figure 1 shows the slit placement of Cecil et al. (2002) on top of an FOC [OIII] image of NGC 1068 from Macchetto et al. (1994). The slits cover an area of 86.4 parsec across and a few thousand parsecs along the slits. However, the brightest emission is seen within a few hundred parsecs of the central engine (CE). Roughly 90% of this NLR emission is covered by the slits with some emission seen outside of slits 1 and 7. We also include slit 8, which is made up of three archival G430M-grating exposures taken in 2000 January and first analyzed by Cecil et al. (2002) (see §1.3). We also overlay a high-resolution MERLIN radio map taken on 1998 January 2. The map was provided in its fully reduced form by Gallimore et al. (2004). With accurate astrometry on the radio data, we can test the correlation between the radio knots and the [OIII] clouds, as was done in Das et al. (2005). We previously found no significant radio interference on the NLR clouds in NGC 4151, such as expansion away from the jet axis, as would be indicated by redshifts and blueshifts of similar magnitude at the radio knot positions.

The high resolution radio map from Gallimore et al. (2004) was scaled to match the pixel resolution of the [OIII] image from Macchetto et al. (1994). We then followed the *HST*

observation procedure for aligning the slits. At the time of observation, slit 4 was centered on the continuum hot spot, and the rest of the slits were offset in the dispersion direction by $0''.2$ (the slit width). Slit 8 (taken by Antonucci) was oriented at a different position angle but was also centered on the hot spot. The intersection of slits 4 and 8 mark the position of the hot spot in Figure 1 (this figure is in [OIII] emission and hence the continuum hot spot is not visible). We then aligned the radio and the [OIII] images by placing radio knot S1 $0''.13 \pm 0''.1$ South and $0''.02 \pm 0''.1$ West of the continuum hot spot. Our motivation stemmed from absolute astrometry studies by Capetti et al. (1997) who placed the optical continuum peak at $\alpha = 02^h42^m40.711^s$, $\delta = -00^\circ00'47''.81$ (J2000) with a precision of 80 mas, and by Muxlow et al. (1996) who placed the radio component S1 at $\alpha = 02^h42^m40.7098^s$, $\delta = -00^\circ00'47''.938$ (J2000) with precision of 20 mas. The central engine, which is presumably the location of the supermassive black hole (SMBH), is now generally accepted to be positioned at S1 because of the observed thermal inverted spectrum between 1.3 cm and 6 cm, and also because of the H₂O maser emission centered on that location (Gallimore et al. 1996; Greenhill & Gwinn 1997; Kumar 1999; Beckert & Duschl 2004). A more detailed treatment of the locations of these and other features in various wave bands is presented by Galliano et al. (2003).

The bottom panel of Figure 1 shows an enlargement of the top panel. The UV and optical continuum hot spot and also NLR-cloud B are found to be coincident within 25 mas; therefore the location of the continuum (‘hot-spot’), shown by the white arrow, is near the dark spot that is NLR-cloud B in this image, in the centers of slits 4 and 8. The radio axis after the bend in the radio jet, is nearly aligned with our slits, extending from knots C to S1. This allows for one-to-one comparison between the radio knots and the [OIII] clouds. Slits 3, 4, and 5 cover most of the radio region and slit 8 captures radio knots S1, S2, and C almost perfectly. It is then easy to extract similar regions of [OIII] and radio data using the slits as a guide.

Figure 2 shows a fully reduced spectral image of the [OIII] $\lambda\lambda 4959, 5007$ emission as it appears through slit 4. The line across the image pointed at by the arrow is the “hot spot” which is presumably produced by nuclear light scattering off of electrons (Crenshaw & Kraemer 2000a). The hidden nucleus is then $0''.13$ south of this optical hot spot and is placed at $0''$ in the image, (see §2).

3. Analysis

Along each slit we extracted one spectrum per pixel in the cross-dispersion direction ($\sim 0''.05/\text{pix}$) and fitted the identifiable component peaks associated with the [OIII] $\lambda 5007$ line with a local continuum and multiple Gaussians. We measured the radial velocities for each component based on the centers of the Gaussian fits. Because we are resolving the [OIII] knots along a slit, we often obtain multiple measurements of the same component. Also the radial velocity may change gradually across a knot of [OIII] gas, suggesting that the knots themselves are made up of smaller clumps or that there are velocity gradients across them. A section of slit 4 shown by the dashed lines across Figure 2 is extracted and fitted with Gaussians as an example. This progression of spectra is shown in Figure 3. The different components for each spectrum are color coded according to the total flux in the line at each location: red for highest flux, blue for medium flux, and black for lowest flux. Such distinction of the components was necessary to compare our models to previous ones in Crenshaw & Kraemer (2000b), since mostly the bright and medium flux knots were detected in their data. Also in Das et al. (2005), the faintest component was found to behave differently than the overall trend of the bright and medium flux components in NGC 4151. We tested for similar flow patterns of the clouds in this paper by tracing the different components. We also measured the position in arcseconds of all components along a slit relative to the center

of that slit¹.

Figures 4, 5, and 6 show the kinematic components in plots of radial velocities, FWHM, and fluxes as a function of projected position from the center of each respective slit. The colors represent the different components as explained previously. In all the radial velocity plots, data points near zero velocity in the range 2–10 arcseconds are in the plane of the galaxy as indicated also by their low FWHM. These points do not play any role in our modeling and are shown only for completeness. For points with larger FWHM, the general trend is an increase in radial velocity from the origin to $\sim 1''.5$, followed by a decrease to the systemic velocity at $\sim 4''$. The fluxes generally decrease away from the CE, with two spikes, one at $\sim 3''.5$ and one at $\sim 8''$, indicating the presence of more gas at these locations, which can be seen in the [OIII] images of Evans et al. (1991). The FWHM does not present any discernible trends in any of the colors except for a slight decrease away from the CE.

For the radio comparison, we first scaled the radio to match the resolution of the [OIII] map. The radio contours were then overlaid on the [OIII] map (Figure 1) to locate the slits that intersect the radio region. The boundaries of the intersecting slits were then used to extract regions along slits 3, 4, 5, and 8 from the radio map. These slits were summed across their widths to find the total intensities along each slit. The radio intensities and the [OIII] data were then plotted against position for each slit, and then compared for any [OIII] disturbance. These results are presented in §5.

Estimates of errors in our measured radial velocities come from three sources. 1) By realizing that the components are not perfect Gaussians, we measured the actual centroid for the $\lambda 5007$ lines of a random sample of spectra and found a maximum fitting error of

¹The center of any slit is defined as the position offset in the dispersion direction from the equivalent value of the pixel that corresponds to the position of the CE in slit 4.

0.89 Å. 2) The finite slit width of $0''.2$ introduces an uncertainty of 0.56 Å for all clouds that are dispersed. 3) Finally, we are limited to how far away from the hot spot we can measure fluxes because of the rapidly degrading signal-to-noise (S/N) ratio. We measured random noisy spectra several times and find that the wavelength shifts vary by ~ 0.25 Å. All these are added in quadrature and converted into velocity to give a maximum error of ± 65 km s $^{-1}$. In all fits, the continuum placement is chosen by eye. We varied the placement of the continuum for randomly selected spectra, but find that the fit is not significantly affected. The S/N ratio of the [OIII] $\lambda 5007$ line rapidly decreases away from the hot spot and we did not measure the emission if the S/N was $\lesssim 3$, which typically occurred at distances of $\gtrsim 6''$. There are also some errors explicit to the separation criteria due to occasional mixing between the medium and low flux components; however such misidentification of the components is small, (see Das et al. 2005 for a full explanation).

4. Kinematic Models

In Crenshaw & Kraemer (2000b), Crenshaw et al. (2000), and Ruiz et al. (2001), models were developed to match the NLRs of NGC 1068, NGC 4151, and Mrk 3. The low-resolution STIS data provided measurements of only the bright NLR clouds and limited spatial coverage of the NLR, since only one or two slit positions were obtained. Therefore, in Das et al. (2005), we reexamined the previous models for NGC 4151 with high-resolution STIS data and full coverage of the NLR. Again in this paper, we use higher dispersion STIS data with large coverage of the NLR to map the kinematics of NGC 1068 and test previous biconical outflow models. Model parameters that we use are listed in Table 1. The parameter z_{max} is measured along the bicone axis from the apex of the model to one end of the bicone (the bicone is symmetrical in geometry about the apex). The parameter v_{max} is the maximum velocity attained by the outflow with respect to the nucleus, and the parameter r_t is the distance

from the nucleus to where the velocity of outflow reaches its maximum. The inner and outer opening angles are actually half-angles, as they are measured from the bicone axis to the inner and outer edges of the bicone respectively. The inclination of the bicone axis is measured with respect to the line-of-sight (LOS) and is zero if the bicone axis is perpendicular to the LOS. Since the [OIII] outflow velocity seems to be following some function-dependent relationship with distance from the nucleus, we used simple velocity laws for the acceleration and deceleration phase of the gas; the ones that worked best were $v = kr$ and $v = v_{\text{max}} - k'r$ respectively, which we collectively refer to as the r law. We tested other velocity laws of the form $v \propto r^n$ but most were not acceptable. One other law matched the data well, our so called \sqrt{r} law, where we used $v = k\sqrt{r}$ for the acceleration and $v = v_{\text{max}} - k'\sqrt{r}$ for the deceleration phase of the gas. The distinction between the two velocity laws is subtle and can be seen in Figure 9 in Das et al. (2005). We continue to use the r law, also referred to as the ‘Hubble Flow’ law by many, in this paper.

Our previous procedure, described in more detail in our past papers, first generated a 2-D radial velocity map based on parameters given in Table 1. For a given parameter set, the velocity field was generated for every increment of angle between the inner and outer opening angles. Normally we used an increment of 1° . Examples of such fields are shown in Figures 5 and 6 in Crenshaw et al. (2000). Samples of radial velocities were then extracted from the model along slit positions, orientations, and widths that matched those of the observations. These velocities were then plotted against position from the center of the respective slit, together with the data points. The parameters were then adjusted slightly and the entire procedure was repeated until we matched the plots of data and model as best as possible, whereby the final parameters are quoted as our best model fit.

In previous models, we used the continuum hot spot as the apex for the biconical outflow of the gas. In this paper we modified the starting point of the outflow to correspond to the

position of the hidden nucleus located $0''.13$ south of the hot spot (Galliano et al. 2003). Although such changes do not affect our final model parameters significantly, we decided to use this location because it is most likely the site of the CE and it might be useful for future dynamical models. Also we want to align as best as possible the radio knots with the positions of the [OIII] clouds, relative to the true center. Such alignment is crucial in testing the radio jet/NLR interactions and the acceleration mechanism of the gas.

In this paper we decided to use a 3-D modeling scheme which is more efficient and greatly reduces our run-time compared to our previous models. In addition the reader can more easily picture and comprehend the biconical outflow geometry. We start by filling in a cubic array with velocities for a given parameter set and velocity law. Note that we fill the cubic array with radial velocities as would be measured by the observer. Such velocities are first determined by our velocity law of outflow and are then converted to radial velocities depending on their positions or coordinates in the model cube. For the purposes of illustration, the radial velocities are then assigned a color based on the amount of redshift or blueshift. Examples of such models are shown in Figure 7. We then take slices through the cube corresponding to slit positions, orientations, and widths that match those of observations. Velocities and positions are then extracted along the slices and plotted together with positions and radial velocities from the observations. Panel (a) in Figure 7 show the velocity field at an inclination of 0° . The parameters that were used to generate the bicone are not the best fit values. They were chosen just for image clarity purposes. Panels (b) and (c) give a clear view of the front and back surfaces respectively of bicone (a). The colors red and blue represent the redshift and blueshift of the surfaces and the key is displayed in panel (g). The darkest blue and red colors in these panels represent the turnover point. This is where the [OIII] gas is at its maximum velocity after which it decelerates back to systemic velocity. Due to the upright orientation of the bicone, gas outflows from its apex are symmetrical above and below. The expected symmetry of the velocities is represented

by the equal color gradients on both front and back surfaces of the bicone. The situation changes when we apply an inclination to the bicone model as in panels (d) and (e). Now the inclination is 5° , with the top toward the observer. Panel (d) is shown with a shaded cross-cut plane that represents the position, orientation, and width of slit 4. One can see slightly higher blueshifts in the top right and slightly higher redshift in the bottom left of (e). The cross section of this plane is shown in panel (e). At each point going up along (e), we extract the range of velocities across the figure and plot those velocities correspondingly in panel (f). Panel (f) represents our final stage for comparing model with real data points. At this stage the model slit as represented by (f) and data points from the corresponding slit are compared. If the fit is found to be unsuitable, the parameters are adjusted slightly and the entire process of generation (d), slit extraction (e), and velocity extraction and plotting (f), undergoes repeated runs until we determine the best match to the data.

5. Results

Figures 8 and 9 show the best fit comparison plots for all eight slits. The models are in shaded gray and the data points in colors, and are plotted with positions relative to the center of the respective slits. These models were done with our best fit parameters listed in Table 2. Previous model parameters found in Crenshaw & Kraemer (2000b) are also listed in that table for comparison. Our results are strikingly consistent with our earlier ones, except that we increase the maximum extent of the bicone and the maximum velocity at turnover point, consistent with the results of Cecil et al. (2002). In addition, the position angle of the bicone was changed from the previously accepted value of 15° (Evans et al. 1991) to 30° , consistent with values derived by Bergeron et al. (1989) and Pogge (1988). This change gave a coherent fit across all eight slits. Slits 5 and 6 cover the same region except for an offset along the slit. They were taken one year apart and show almost identical data points. The

difference is seen mostly in the low and medium flux clouds, which can be attributed to our separation criteria for distinguishing the different kinematic components (see §3).

The fit to the bright and most medium flux clouds is relatively good. Note that the long line of red points near zero velocity in the northeast are points in the host galaxy which were not fitted. These points are actually low absolute flux and low FWHM points detected with only one kinematic component per location. Because of this, our separation routine assigned the color red to these points, but clearly these points are not in any outflow pattern. There are also some faint clouds outside of the bicone geometry around zero position in all slits that are not fit. We present an explanation in terms of the radio jet for this sort of flow pattern of the fainter clouds in §6.

The trend in all slits is that the points accelerate then decelerate with approximately linear velocity laws. The sparsity of points enclosed by, but not in, the shaded regions of Figures 8 and 9 indicate that the bicone interior is hollow. Slit 8 does not show this hollowed out area as the rest of the slits, because it is placed at a position angle of 10° (as opposed to 38° for the rest of the slits), which makes it lie along one edge of the bicone. For all the slits, the data follow the models quite well in the northeast, even for slit 8, where the data seem to agree with the filled shaded configuration reasonably well.

The lack of data points in the southwest can be explained by the shielding of the bicone by the host galaxy, as shown in Figure 10. Our model predicts that the outer half-opening-angle of the bicone is 40° , with the northeast side inclined at 5° out of the plane of the sky. This decreases the opening angle of the southwest side relative to the plane of the sky by 5 degrees. The host galaxy is inclined by 40° (de Vaucouleurs et al. 1991), thus effectively placing more material between us and the southwest side of the bicone. The northeast side of the bicone is therefore above the galactic disk. Studies of HI absorption in NGC 1068 (Gallimore et al. 1994) find that the NE radio jet is also in front of the galactic disk, which

is consistent with our result. Both the northeast far side, and the southwest near side of the bicone are flowing in/near the galactic plane. Such interaction between gas in the host galaxy and ionizing radiation in the bicone is responsible for carving out the morphology of the Extended Narrow Line Region (ENLR).

Figure 11 is a plot of relative radio intensities along slits 2, 3, 4, and 8, together with [OIII] radial velocities within $2''$ of the CE. In panel 1 (slit 3) of this figure, the radio knot (S2) does not seem to have any effect on the bright cloud velocities, i.e., the bright points are not convincingly split into redshifts and blueshifts at S2. Furthermore the narrow range of the radio emission cannot account for the slowly but steadily increasing blueshifted velocity going from $0''.5$ to $-0''.5$. At radio knot S1 in panel 2 (slit 4), there seem to be splitting of the velocities, but this splitting extends all the way beyond $-0''.2$, where there is no radio. The splitting of the bright clouds continues after radio knot NE, going to the right. Similar scenarios apply to panels 3 and 4; the bright clouds split in velocities, but not preferentially at the position of the radio knots.

The fainter clouds at the positions of the radio knots in Figure 11, however, portray a different picture. The green circles represent pairwise velocity splitting where the radio knots are strongest. The split velocities have approximately equal magnitudes in redshifts and blueshifts, and the splitting is seen only in the low and medium flux clouds, but not in the high flux clouds. At radio knot C in panels 2, 3, and 4, there is minimal splitting, with low velocities. This could be due to the fact that the radio jet bends at this position, after colliding with [OIII] cloud C. The blue circles represent faint clouds for which there is no corresponding blueshifted velocity split. These pairwise splitting of velocities is explained in terms of lateral expansion of the radio jet in §6.

6. Discussion

We compared our previous kinematic models for NGC 1068 with our current ones in this paper and found that they remained consistent. Radial outflow of the [OIII] clouds can explain the general large-scale flow pattern of the narrow-line regions of both types of Seyfert galaxies, such as NGC 4151 from Das et al. (2005) and NGC 1068 from the current paper. However the models are not a perfect match, and further insight can be gained from the discrepancies seen in Figures 8 and 9. Superimposed on the general trend of the flow, there are a number of clouds with peculiar velocities not in the shaded regions of our model. Points near systemic velocity that extends from $\sim 2''$ to $\sim 9''$ are faint clouds in the host galaxy, on the far side of the northeast cone, as shown in Figure 10.

High-velocity points near $0''$ are also not in the shaded region of our biconical model and may not be affected by processes that drive the outflow of the bright clouds along the bicone. These points can possibly be explained by lateral expansion of hot gas away from the radio jet, as claimed by Axon et al. (1998) and Capetti et al. (1997). Figure 12 shows a schematic of this lateral expansion of fainter clouds away from the jet/bicone axis. This flow however is restricted to clouds within a few tens of parsecs from the CE, along the region of the radio jet. The large scale outflow of the bright clouds cannot be accounted for by the radio, and needs a different acceleration process. The evidence for a small scale lateral flow was previously shown in Figure 11 as velocity splitting of the faint clouds at the positions of the radio knots, in §5. Another possible explanation is that these clouds may be driven by radiation escaping through a patchy torus or by scattered light, which would also explain their ionization outside of the classic bicone structure (e.g., see Kraemer & Crenshaw 2000a). Schmitt et al. (2006) has shown that these clouds indeed have a lower ionization state than those in the bicone, indicating a patchy torus or at least a much lower extinction column than that in the LOS. Recent models of the IR emission from the putative torus in Seyfert

galaxies also indicate a patchy geometry (e.g., Nenkova et al. 2002).

The large scale outflow itself is not well understood dynamically. The gas seems to accelerate out to about 140 pc, then decelerate back to systemic velocity. Such a flow pattern was observed in several other Seyferts by our group. Mrk 3 shows a turnover in velocity at ~ 80 pc and NGC 4151 shows turnover at ~ 96 pc. Whatever is slowing the gas down is not known for certain, but we suspect that it might be diffuse, possibly X-ray emitting, gas in the ambient medium. The most likely driving mechanism, radiation pressure by line driving, has some drawbacks. Models developed by Everett (2005) predict that the gas should reach high velocities very close in, at $\lesssim 1$ pc. Gas is lifted off the accretion disk by magnetocentrifugal and radiative forces, and then driven by radiation. Part of the lifted gas is used for shielding, to avoid complete ionization of the driven gas. The model, however, cannot match our results because the observed acceleration of the gas is much shallower than that predicted by the model, attaining maximum radial velocity at ~ 100 pc, whereas the model predicts maximum velocity within ~ 1 pc.

The large scale flow of the NLR clouds is not likely to be accelerated radially by the radio jet. Considering that the density the radio knots is of the order $\sim 10^{-5}$ cm $^{-3}$ and that of the [OIII] clouds is $\sim 10^5$ cm $^{-3}$, momentum arguments and the large solid angle covered by the [OIII] clouds would make it difficult for the radio jet to push the clouds to high velocity. Mundell et al. (2003) suggests that some NLR clouds are actually responsible for bending the radio jet. For example, NLR knot C is most likely responsible for the bend in the radio jet at radio knot C (Capetti et al. 1999).

We have shown that the lateral expanding cocoon model (Axon et al. 1998; Capetti et al. 1997) cannot be the main driving mechanism for the NLR clouds in NGC 1068. Furthermore, it cannot account for the kinematics of the Seyfert 1 galaxies NGC 4151 (Crenshaw & Kraemer 2000b) and NGC 3516 (Ruiz et al. 2005). These galaxies unambiguously show

redshifts on one side and blueshifts on the other side the nucleus, contradicting the lateral expansion model, which predicts redshifts and blueshifts on both sides of the nucleus, regardless of inclination of the bicones. However, the radio jet in itself could be responsible for clearing a channel through the center of the bicone, providing the hollowed out interior that matches our models, as stated in our earlier papers. Also, the lateral expansion of the radio knots in NGC 1068 may be responsible for pushing the fainter clouds aside, filling in the apex in our biconical models with low ionization gas.

We thank J.F. Gallimore for providing the high resolution MERLIN radio map of NGC 1068 used in this study. Some of the data presented in this paper were obtained from the Multimission Archive at the Space Telescope Science Institute (MAST). STScI is operated by the Association of Universities for Research in Astronomy, Inc., under NASA contract NAS5-26555. This research has made use of NASA’s Astrophysics Data System.

REFERENCES

- Antonucci, R. R. J. & Miller, J. S. 1985, *ApJ*, 297, 621
- Arribas, S., Mediavilla, E., & Garcia-Lorenzo, B. 1996, *ApJ*, 463, 509
- Axon, D. J., Marconi, A., Capetti, A., Macchetto, F. D., Schreier, E., & Robinson, A. 1998, *ApJ*, 496, L75
- Beckert, T. & Duschl, W. J. 2004, *A&A*, 426, 445
- Bergeron, J., Petitjean, P., & Durret, F. 1989, *A&A*, 213, 61
- Bland-Hawthorn, J., Gallimore, J. F., Tacconi, L. J., Brinks, E., Baum, S. A., Antonucci, R. R. J., & Cecil, G. N. 1997, *Ap&SS*, 248, 9
- Brinks, E., Skillman, E. D., Terlevich, R. J., & Terlevich, E. 1997, *Ap&SS*, 248, 23
- Capetti, A., Axon, D. J., Macchetto, F. D., Marconi, A., & Winge, C. 1999, *ApJ*, 516, 187
- Capetti, A., Macchetto, F. D., & Lattanzi, M. G. 1997, *ApJ*, 476, L67
- Cecil, G., Dopita, M. A., Groves, B., Wilson, A. S., Ferruit, P., Pécontal, E., & Binette, L. 2002, *ApJ*, 568, 627
- Crenshaw, D. M. & Kraemer, S. B. 2000a, *ApJ*, 532, 247
- . 2000b, *ApJ*, 532, L101
- Crenshaw, D. M., Kraemer, S. B., Hutchings, J., Bradley II, L. D., Gull, T. R., Kaiser, M. E., Nelson, C. H., Ruiz, J. R., & Weistrop, D. 2000, *ApJ*, 120, 1731
- Das, V., Crenshaw, D. M., Hutchings, J., Deo, R. P., Kraemer, S. B., Gull, T. R., Kaiser, M. E., Nelson, C. H., & Weistrop, D. 2005, *AJ*, 130, 945

- de Vaucouleurs, G., de Vaucouleurs, A., Corwin, H. G., Buta, R. J., Paturel, G., & Fouque, P. 1991, Third Reference Catalogue of Bright Galaxies (Volume 1-3, XII, 2069 pp. 7 figs.. Springer-Verlag Berlin Heidelberg New York)
- Dopita, M. A. & Sutherland, R. S. 1995, *ApJ*, 455, 468
- Evans, I. N., Ford, H. C., Kinney, A. L., Antonucci, R. R. J., Armus, L., & Caganoff, S. 1991, *ApJ*, 369, L27
- Evans, I. N., Tsvetanov, Z., Kriss, G. A., Ford, H. C., Caganoff, S., & Koratkar, A. P. 1993, *ApJ*, 417, 82
- Everett, J. E. 2005, *ApJ*, 631, 689
- Ferland, G. J. & Osterbrock, D. E. 1986, *ApJ*, 300, 658
- Galliano, E., Alloin, D., Granato, G. L., & Villar-Martín, M. 2003, *A&A*, 412, 615
- Gallimore, J. F., Baum, S. A., & O’Dea, C. P. 1996, *ApJ*, 464, 198
- . 2004, *ApJ*, 613, 794
- Gallimore, J. F., Baum, S. A., O’Dea, C. P., Brinks, E., & Pedlar, A. 1994, *ApJ*, 422, L13
- Greenhill, L. J. & Gwinn, C. R. 1997, *Ap&SS*, 248, 261
- Greenstein, J. L. & Schmidt, M. 1964, *ApJ*, 140, 1G
- Groves, B. A., Cecil, G., Ferruit, P., & Dopita, M. A. 2004, *ApJ*, 611, 786
- Kay, L. E. 1994, *ApJ*, 430, 196
- Koski, A. T. 1978, *ApJ*, 223, 56
- Kraemer, S. B. & Crenshaw, D. M. 2000a, *ApJ*, 532, 256

———. 2000b, *ApJ*, 544, 763

Kraemer, S. B., Crenshaw, D. M., Hutchings, J. B., Gull, T. R., Kaiser, M. E., Nelson, C. H.,
& Weistrop, D. 2000, *ApJ*, 531, 278

Kumar, P. 1999, *ApJ*, 519, 599

Lumsden, S. L., Heisler, C. A., Bailey, J. A., Hough, J. H., & Young, S. 2001, *MNRAS*, 327,
459

Macchetto, F., Capetti, A., Sparks, W. B., Axon, D. J., & Boksenberg, A. 1994, *ApJ*, 435,
L15

Miller, J. S. & Goodrich, R. W. 1990, *ApJ*, 355, 456

Moran, E. C., Barth, A. J., Kay, L. E., & Filippenko, A. V. 2000, *ApJ*, 540, L73

Mundell, C. G., Wrobel, J. M., Pedlar, A., & Gallimore, J. F. 2003, *ApJ*, 583, 192

Muxlow, T. W. B., Pedlar, A., Holloway, A. J., Gallimore, J. F., & Antonucci, R. R. J. 1996,
MNRAS, 278, 854

Nelson, C. H., Weistrop, D., Hutchings, J. B., Crenshaw, D. M., Gull, T. R., Kaiser, M. E.,
Kraemer, S. B., & Lindler, D. 2000, *ApJ*, 531, 257

Nenkova, M., Ivezić, Ž., & Elitzur, M. 2002, *ApJ*, 570, L9

Oke, J. B. 1965, *ApJ*, 141, 60

Osterbrock, D. E. & Parker, R. A. R. 1966, *ApJ*, 143, 268O

Pogge, R. W. 1988, *ApJ*, 328, 519

Ruiz, J. R., Crenshaw, D. M., Kraemer, S. B., Bower, G. A., Gull, T. R., Hutchings, J. B.,
Kaiser, M. E., & Weistrop, D. 2001, *AJ*, 122, 2961

———. 2005, *AJ*, 129, 73

Schmitt, H. R. & Kinney, A. L. 1996, *ApJ*, 463, 498

Schmitt, H. R., Kraemer, S. B., Crenshaw, D. M., & Hutchings, J. B. 2006, in *The X-ray Universe 2005 (ESA)*, proceedings, in press

Schulz, H. 1990, *AJ*, 99, 1442

Tran, H. D. 2001, *ApJ*, 554, L19

Tran, H. D., Miller, J. S., & Kay, L. E. 1992, *ApJ*, 397, 452

Walker, M. F. 1968, *ApJ*, 151, 71

Young, S., Hough, J. H., Axon, D. J., Ward, M. J., & Bailey, J. A. 1996, *MNRAS*, 280, 291

Young, S., Hough, J. H., Bailey, J. A., Axon, D. J., & Ward, M. J. 1993, *MNRAS*, 260, L1

Zakamska, N. L., Schmidt, G. D., Smith, P. S., Strauss, M. A., Krolik, J. H., Hall, P. B., Richards, G. T., Schneider, D. P., Brinkmann, J., & Szokoly, G. P. 2005, *AJ*, 129, 1212

Fig. 1.— Top: Faint Object Camera(FOC)/Corrective Optics Space Telescope Axial Replacement(COSTAR) log intensity [OIII] image of the NLR of NGC 1068 shown with the orientation and position of the seven overlying slits. The image was taken through the narrow-band filter (F501N), and the slits are those of STIS observations. The position angle of slits 1–7 on the sky is 38° , and slit 8 is at 10° . Contours are from the radio image. Bottom: Enlarged view of the white box from top showing the radio region with the slits overlaid. Note that slits 3, 4, and 5 cover the strong radio knots, while slit 8 redundantly covers radio knots C, S1, and S2. The center of the continuum hot spot is found at the intersection of slits 4 and 8 as shown by one of the white arrows, while the other white arrows point to known radio knots. Radio knot S1 marks the position of the SMBH.

Fig. 2.— [OIII] $\lambda 4959,5007$ dispersed image of slit 4. The arrow points to the optical continuum hot spot. The hidden nucleus is positioned at zero arcsecond slightly below the continuum. The dotted lines across the image represent the region of extraction for the progression of spectra in Figure 3. This progression goes up the slit.

Fig. 3.— Progression of spectra from slit 4 (see Figure 2) showing the fluctuation of [OIII] components with position along the slit, together with the summed gaussian fits. These components are separated according to total relative flux in the lines and are color coded red (R), blue (B), and black (K), for high, medium, and low flux, respectively.

Fig. 4.— Plots of radial velocity, FWHM, and flux, from slits 1–3, showing multiple components at each position along the slit. Red represents the highest flux component, blue the medium flux component, and black the lowest flux component for each position. An example of the separation is shown in Figure 3.

Fig. 5.— Same as in Figure 4, but for slits 4–6.

Fig. 6.— Same as in Figure 4, but for slits 7–8.

Fig. 7.— Bicone models showing the velocity fields for two slightly different inclinations. Panel (a) shows the 3-D structure of the model with no inclination with the arrow indicating the line-of-sight. Panels (b) and (c) show the front and back part respectively of the (a) as it would appear in the sky in terms of radial velocity measurements. Panels (d), (e), and (f) show our kinematic model for NGC 1068 and our slit extraction procedure. The shaded plane in panel (d) mimics the position of slit 4 and panel (e) shows the extracted velocities along that plane. Panel (f) is a corresponding shaded plot of velocities from (e). Panel (g) gives a radial velocity key for models (a), (b), and (c). The inclination of (d) changes its maximum redshift and blueshift from that indicated by the key; see section 4 for more details.

Fig. 8.— Models in shaded grey and data points in colors showing the fit for slits 1–4. The southwest side of the cone is likely extinguished by dust in the plane of the host galaxy. The continuous string of points in the northeast near 0 km s^{-1} , as well as similar points in the southwest at many positions, are velocities from clouds in the host galaxy. The colors red, blue, and black are defined similarly as in Figures 3 and 4.

Fig. 9.— Same as in Figure 8 but for slits 5–8. Slits 5 and 6 differ only by a vertical offset. The small differences in some of the radial velocity data points may be due to noise and in the way we separate the various kinematic components. Slit 8 shows a wide range of velocities both by model and data. The low and medium flux points at a range of velocities near $0''$ are outside of our bicone geometry, as discussed in the text.

Fig. 10.— Plot showing the orientation of the bicone relative to the host galaxy as they would appear in the sky. Parts of the southwest bicone are being blocked by the galactic disk of NGC 1068, hence the lack of data points in the southwest in Figures 8 and 9.

Fig. 11.— Plots of relative radio intensities superposed on [OIII] radial velocity plots. The

colors of the velocity points are defined as in Figure 3. These are the only slits that intercept the radio.

Fig. 12.— Cartoon showing the bicone geometry of the NLR with the radio jet in the center in dark color. Lateral expansion due to the radio knots is driving fainter NLR clouds perpendicular to the bicone axis, independent of the large scale flow of the bright clouds. The apex of the bicone therefore becomes broadened.

Table 1. DEFINITION OF MODEL PARAMETERS

Parameter	Symbol
Maximum distance along bicone axis	z_{\max}
Inner opening angle	θ_{inner}
Outer opening angle	θ_{outer}
Inclination of bicone axis	i_{axis}
Position angle of bicone axis	PA_{axis}
Maximum velocity ^a	v_{\max}
Turnover distance ^a	r_{t}

^adeprojected: i.e relative to the nucleus, not the observer

Table 2. KINEMATIC MODEL OF NGC 1068

Parameter	Previous ^a	This Paper
$z_{\max}(\text{pc})$	306	400 ± 16
$\theta_{\text{inner}}(\text{deg})$	26	20 ± 2
$\theta_{\text{outer}}(\text{deg})$	40	40 ± 2
$i_{\text{axis}}(\text{deg})$	5 ^b	$5 \pm 2^{\text{b}}$
$PA_{\text{axis}}(\text{deg})$	15	30 ± 2
$v_{\max}(\text{ km s}^{-1})$	1300	2000 ± 50
$r_{\text{t}}(\text{pc})$	137	140 ± 10

^aCrenshaw & Kraemer (2000b)

^bnortheast is closer

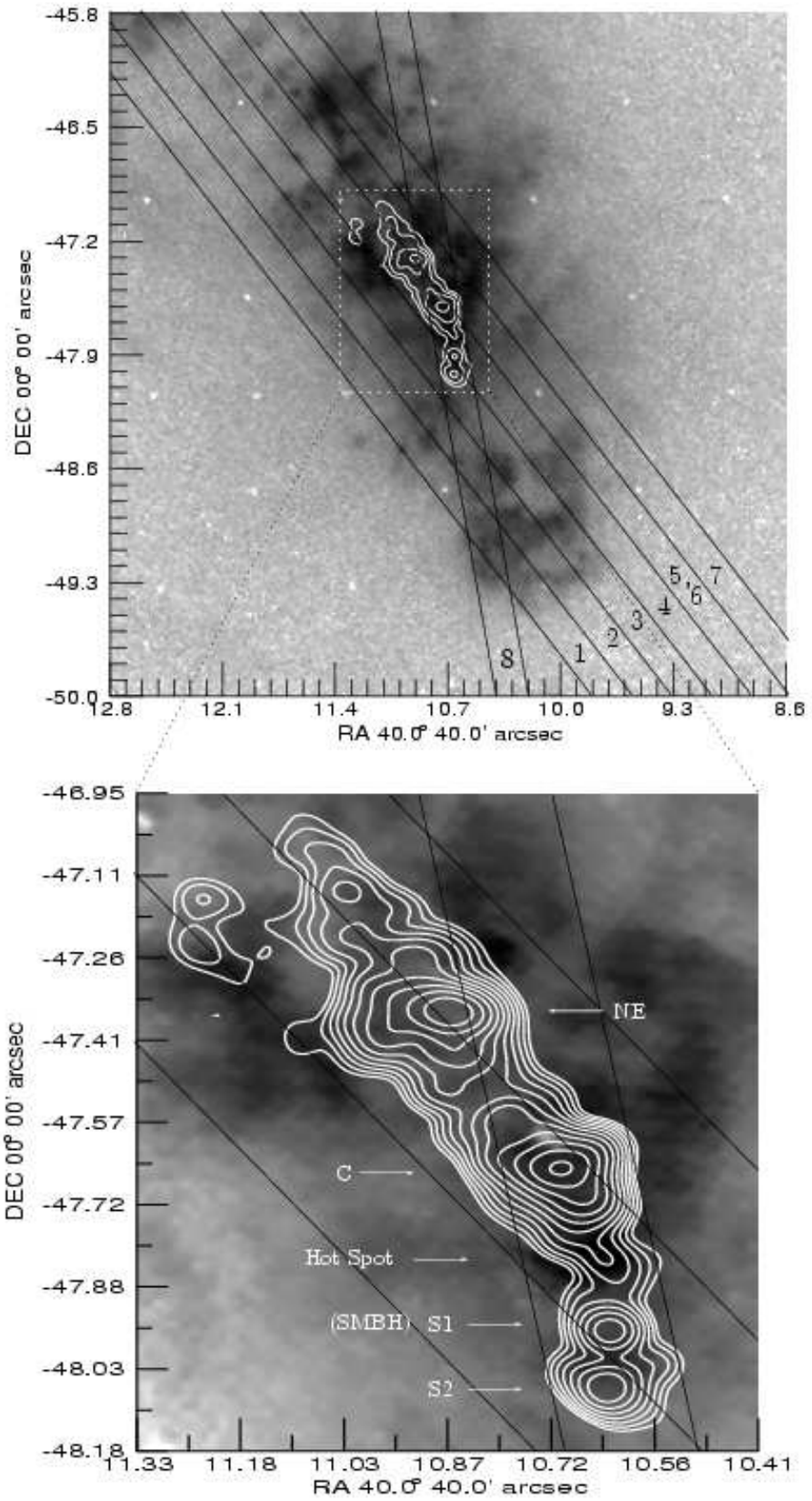


Fig. 1

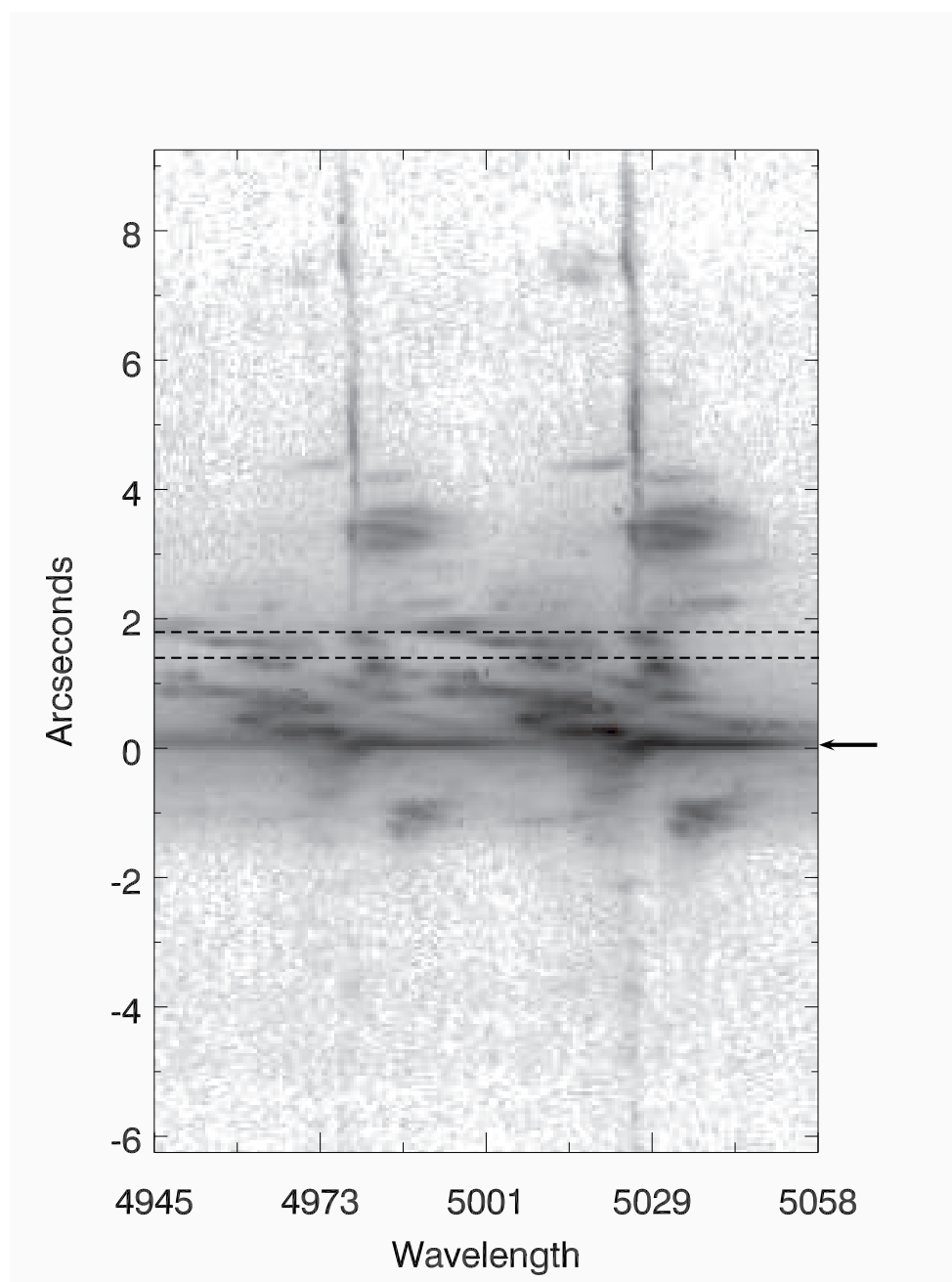


Fig. 2

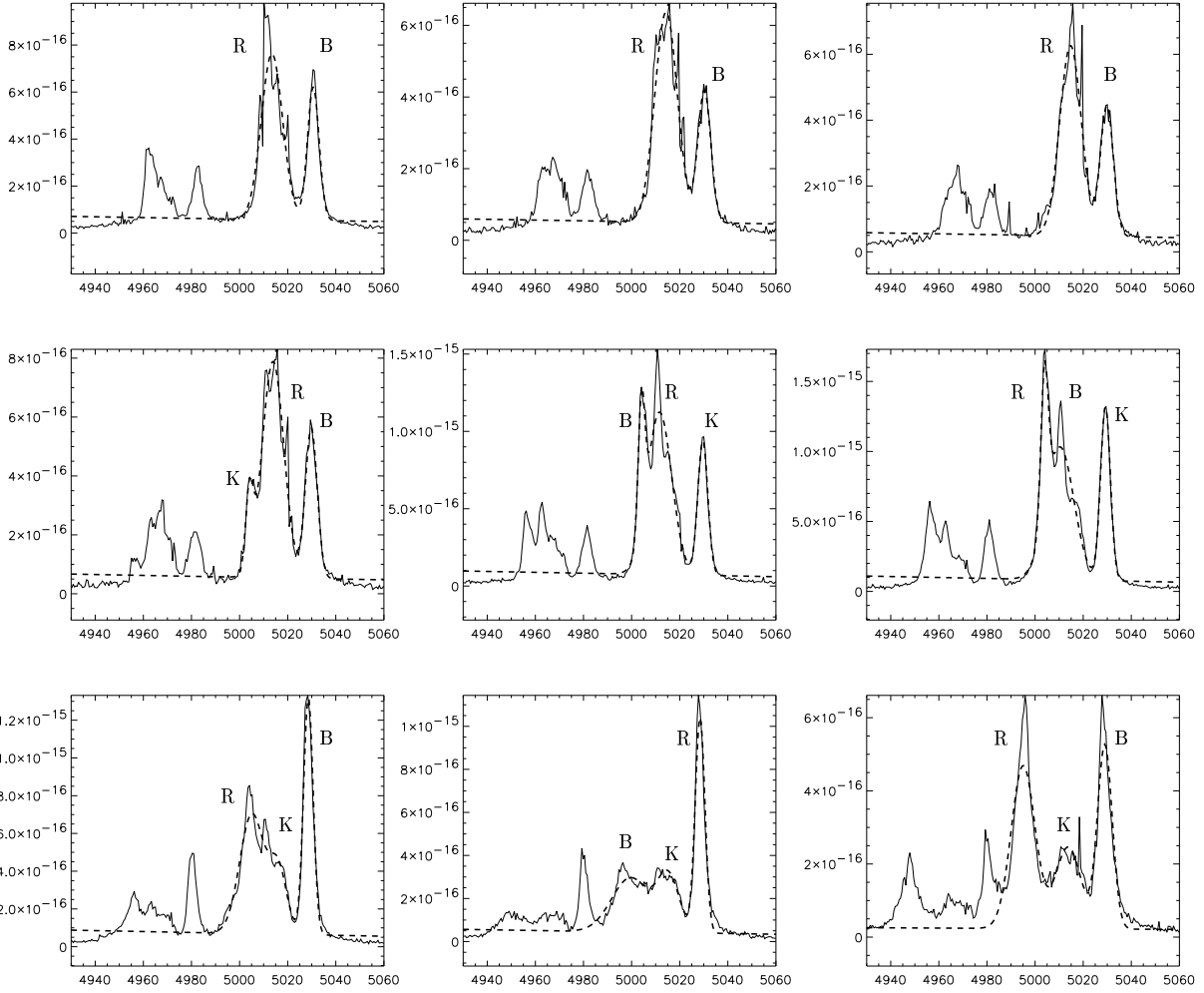


Fig. 3

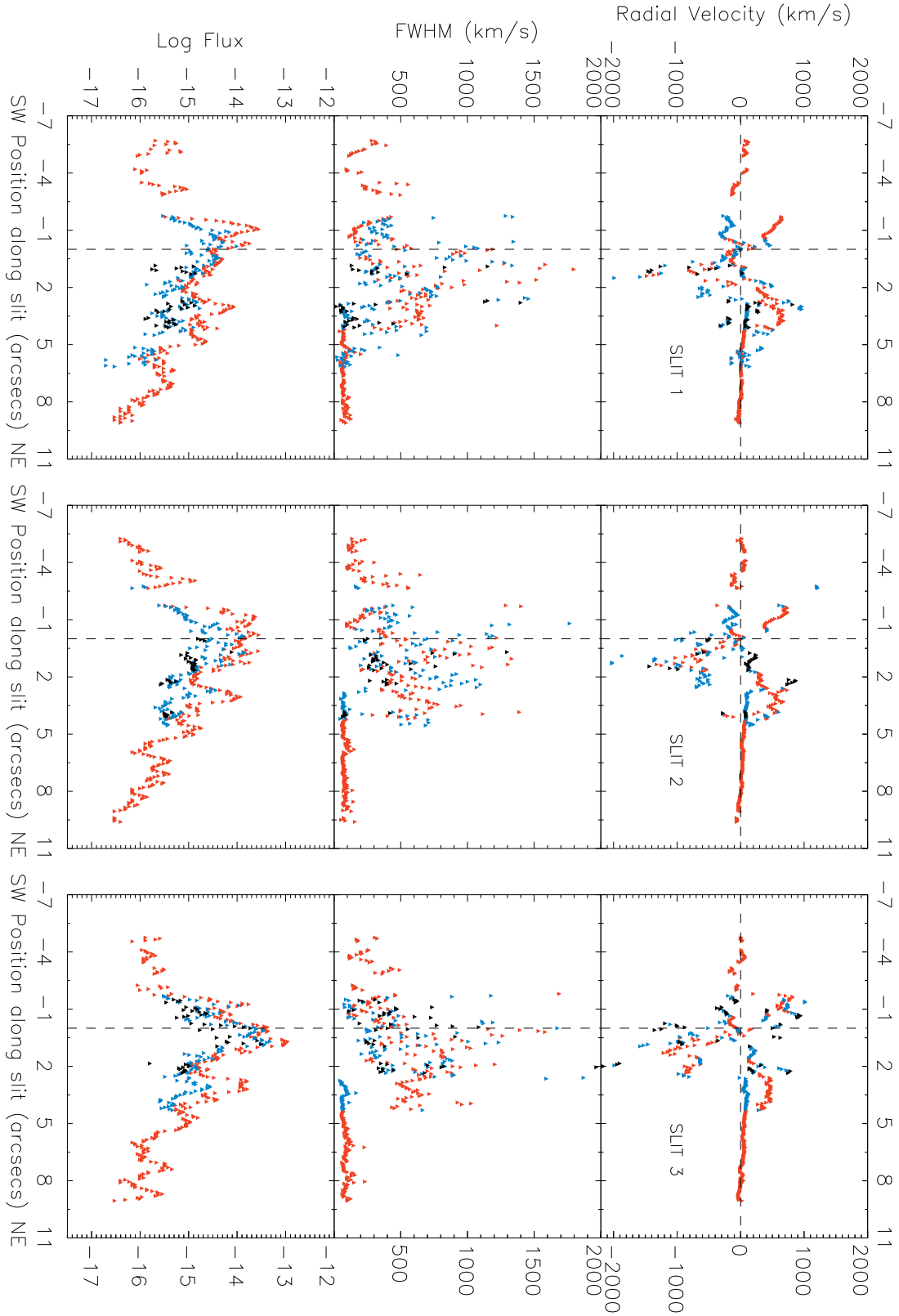


Fig. 4

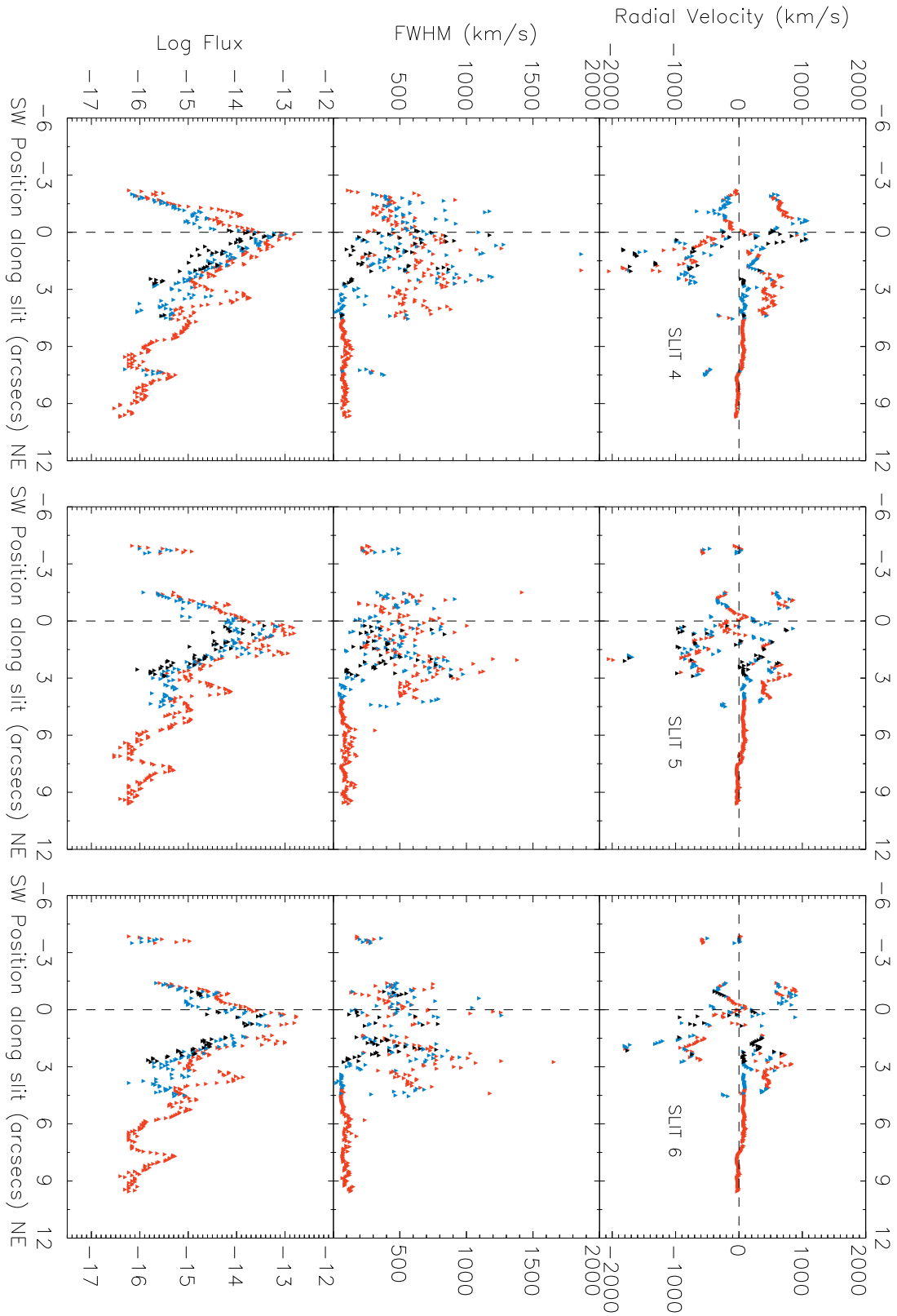


Fig. 5

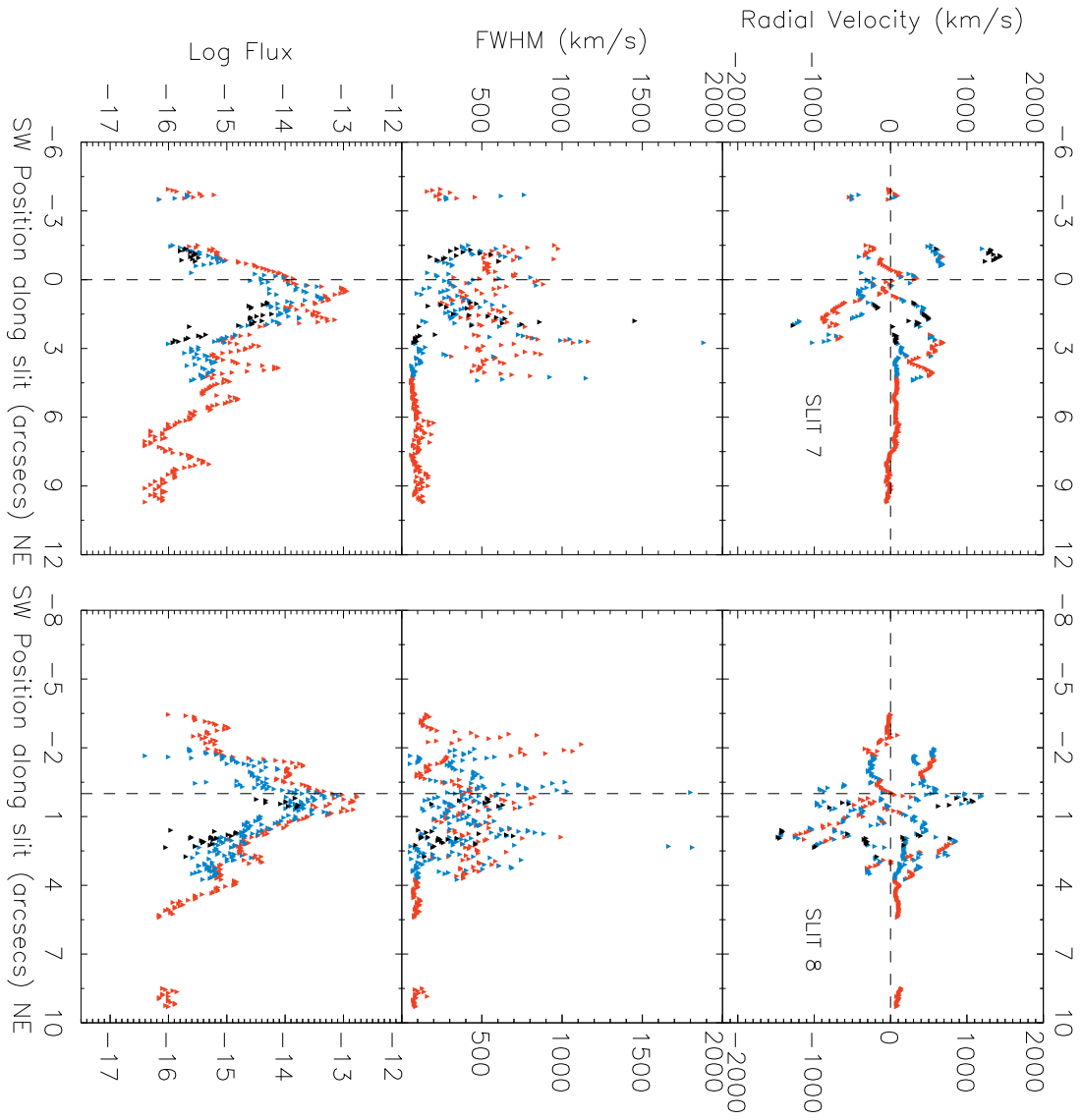


Fig. 6

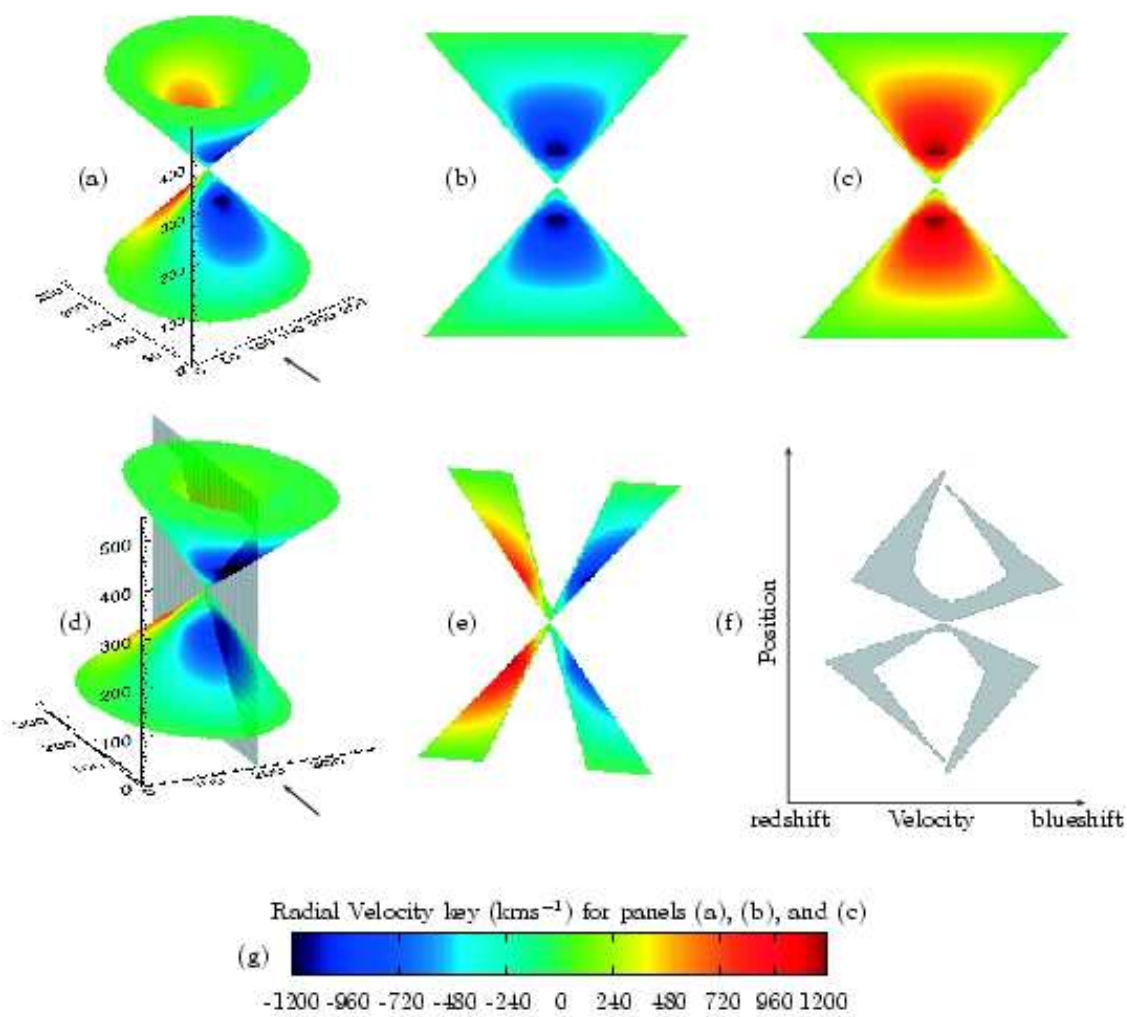


Fig. 7

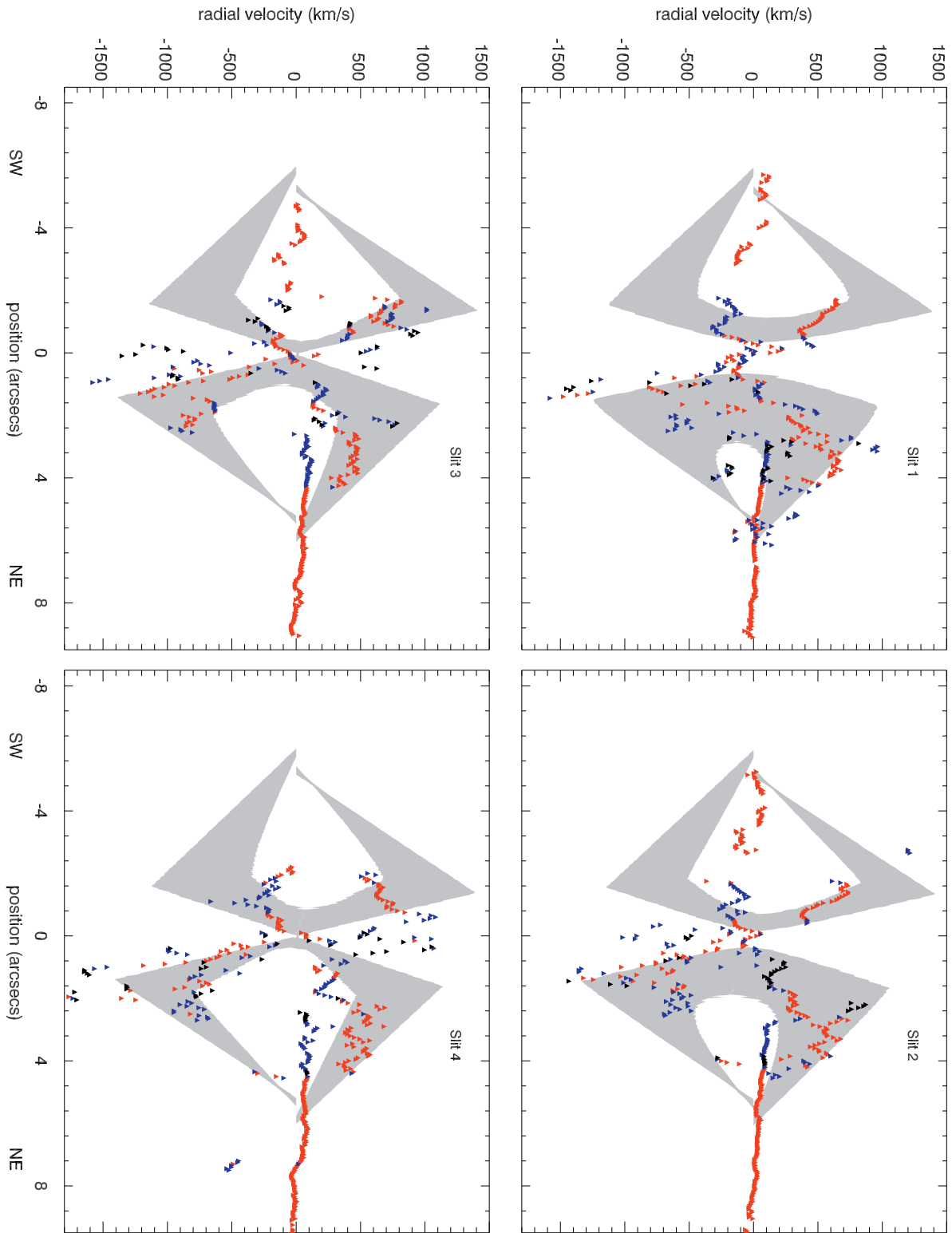


Fig. 8

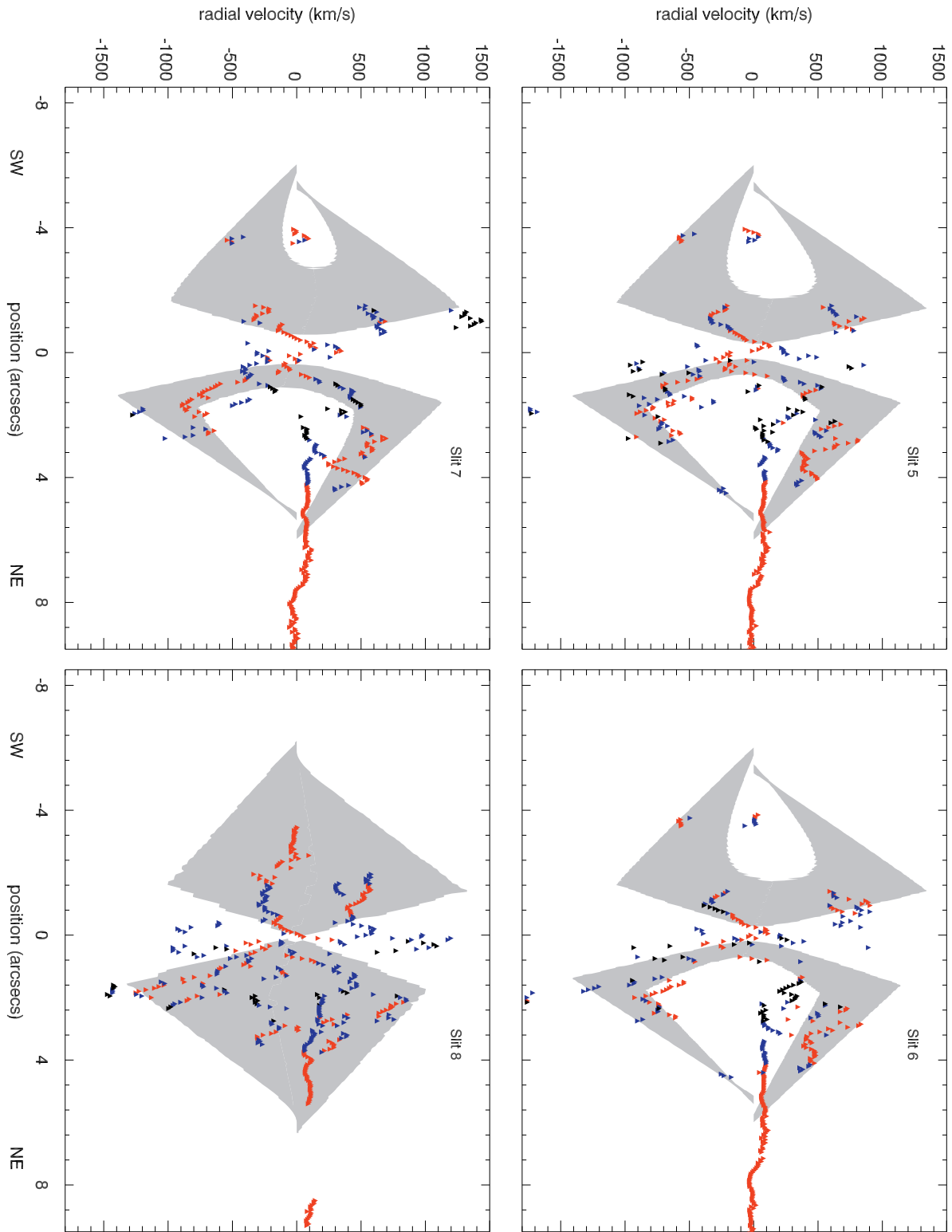


Fig. 9

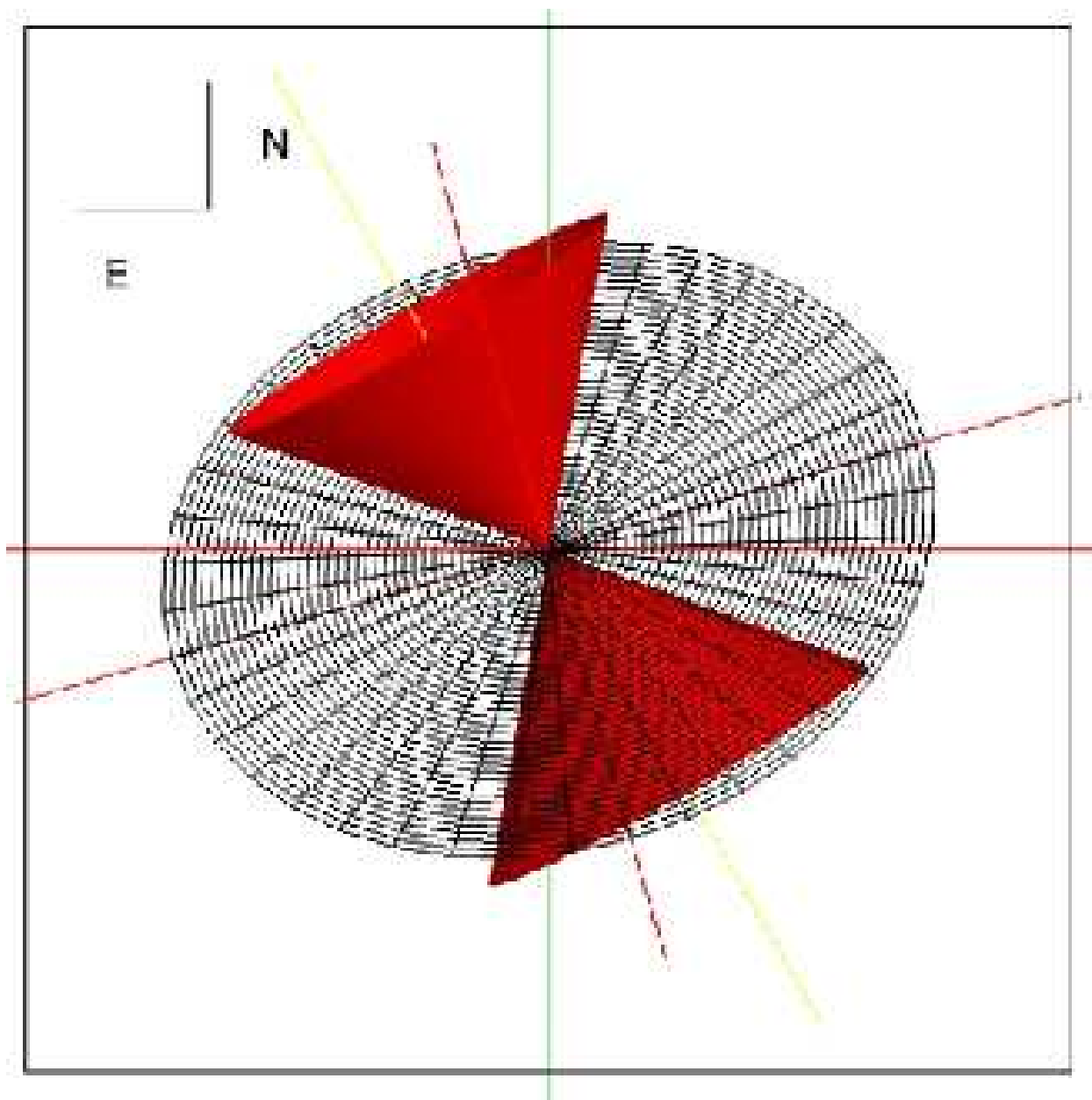


Fig. 10

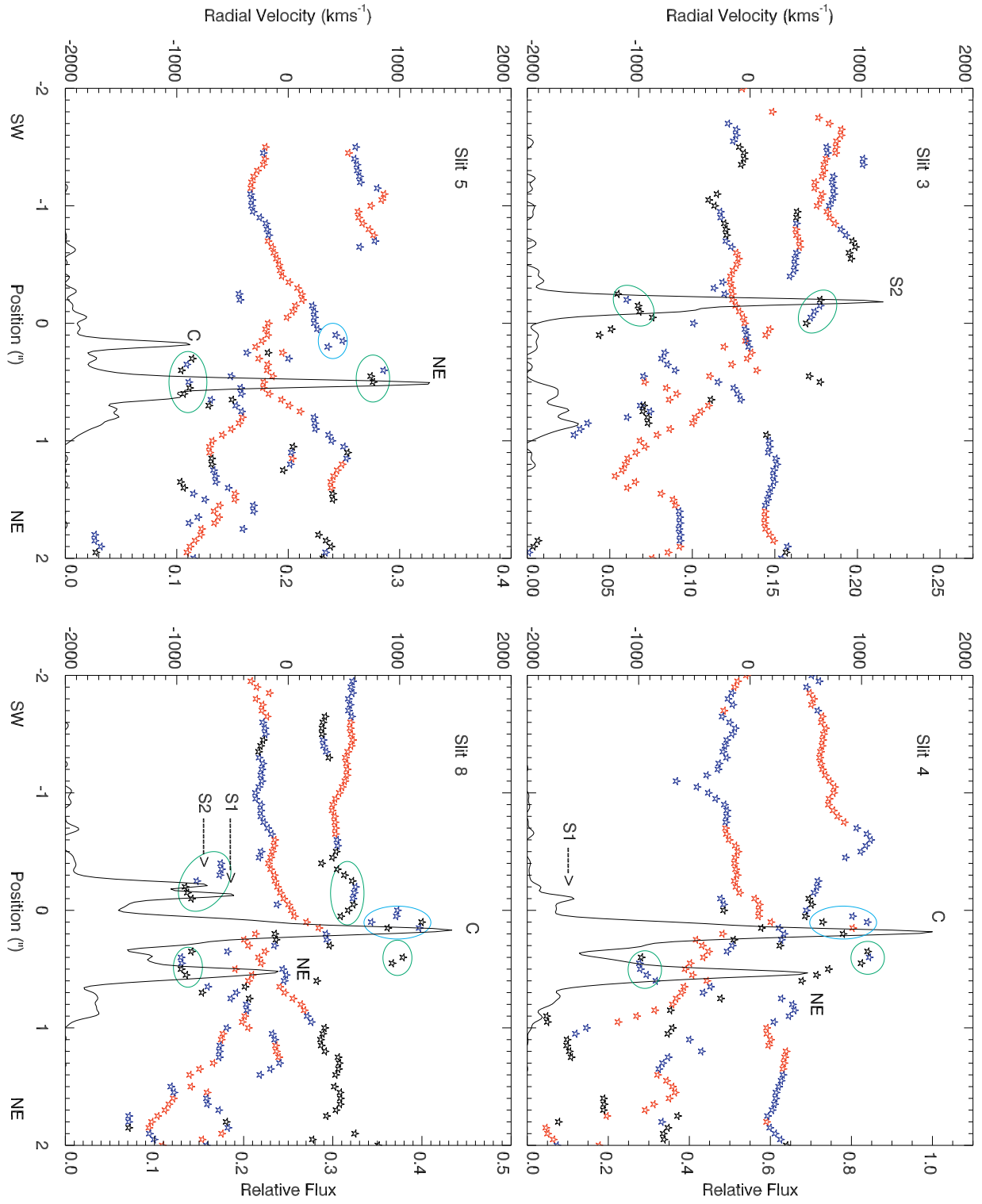


Fig. 11

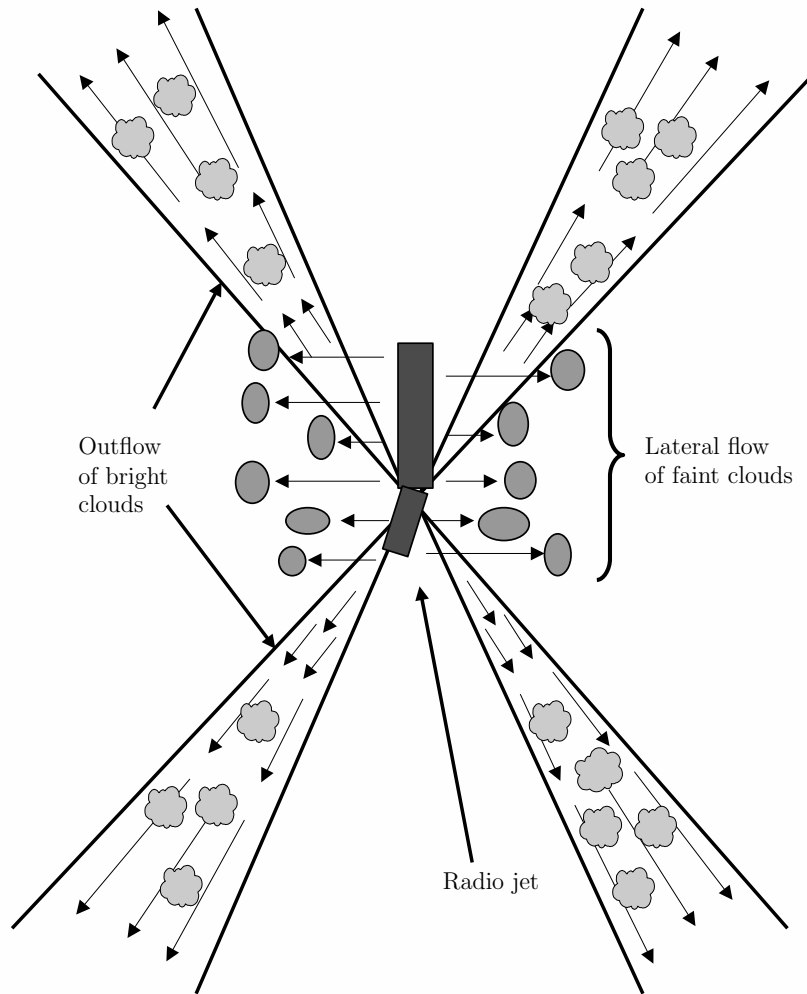


Fig. 12